Microscopic structure of interfaces in $Si_{1-x}Ge_x/Si$ heterostructures and superlattices studied by x-ray scattering and fluorescence yield

Z. H. Ming, A. Krol, Y. L. Soo, and Y. H. Kao
Department of Physics, State University of New York at Buffalo, Buffalo, New York 14260

J. S. Park and K. L. Wang
Electrical Engineering Department, University of California, Los Angeles, California 90024
(Received 21 January 1993)

The angular dependences of grazing-incidence x-ray scattering and Ge $K\alpha$ fluorescence yield were measured for $Si_{1-x}Ge_x/Si$ and its inverted $Si/Si_{1-x}Ge_x$ heterostructures. The results reveal useful information on microstructures in these layered materials and show similar interfacial structures in terms of the rms interfacial roughness, correlation length of height fluctuations, and Ge density profile. Two ten-period superlattices with different thickness and Ge concentration were also investigated; correlation between height fluctuations of different interfaces is clearly demonstrated in the data of x-ray-diffuse scattering. These results show that x-ray scattering and fluorescence techniques can be employed as convenient tools for nondestructive characterization of epilayer thickness, interfacial roughness, density profile of selected atomic species, and correlations between microstructures of different interfaces in layered materials.

I. INTRODUCTION

Recently there has been considerable interest in the properties of epitaxially grown strained-layer superlattices (SLS's) of $Si_{1-x}Ge_x/Si$ due to their potentially important applications in various integrated optoelectronic and field-effect-transistor devices.[1-3] Although the lattice mismatch between Ge and Si is about 4%, high-quality heterostructures and superlattices of $Si_{1-x}Ge_x$ can still be grown free of misfit dislocations as the lattice mismatch can be accommodated by coherent strains. The strains in a SLS may dramatically alter its optical and electronic properties, thereby providing an efficient means for band-structure engineering.[4] Since the quality of interfaces can greatly influence the strain and electron transport in thin-layer heterostructures,[5] a detailed knowledge of interfacial microstructure is of central importance for understanding the properties of layered materials. For example, it has been demonstrated recently that the carrier mobility is indeed limited by interfacial roughness scattering in thin quantum-well structures.[6]

Prior to the applications of x-ray scattering and fluorescence techniques, interfaces have been studied previously using other methods, such as high-resolution transmission electron microscopy,[7] photoluminescence (PL),[8] transport measurements,[6] and Raman scattering.[9] Some of these techniques suffer the limitations of being either destructive or depending on the quantitative details of the exciton spectra. For semiconductors in which the exciton size is about 100 Å, small interfacial roughness around 10 Å cannot be accurately resolved from the PL measurements. Furthermore, in some of these techniques, e.g., the PL linewidth, it is difficult to differentiate the contributions due to interfacial roughness from that caused by changes in the material properties.

On the other hand, x-ray measurements are sensitive to the spatial variation of the refractive indices, which is directly related to the electron density of the material under study; thus x ray can provide detailed and element-specific structural information on selected atomic species. The advent of intense x rays from synchrotron radiation makes the x-ray techniques more useful for studying the microstructure of interfaces. In the present work, both grazing-angle x-ray scattering and fluorescence techniques are applied to a study of the $Si_{1-x}Ge_x$ system, with an emphasis on the difference in interfacial roughness between normal ($Si_{1-x}Ge_x$ on Si) and inverted (Si on $Si_{1-x}Ge_x$) heterostructures. An understanding of the difference between the normal and inverted structures is generally believed to be useful for the study of superlattices and the strain accommodated therein during epitaxial growth.

II. THEORY

The effects of x ray on materials are commonly characterized by a complex refractive index[10] $n=1-\delta-i\beta$, where δ and β are the optical constants related to the atomic scattering factor and electron density of the material. The magnitude of optical constant δ is usually on the order of 10^{-6} and β is about an order smaller than δ for hard x ray.[11] For x ray with wavelength λ ($=hc/E$) the optical constants can be expressed as

$$\delta=\frac{r_0}{2\pi}\lambda^2 N_A\sum_i\frac{\rho_i}{A_i}(Z_i+f_i'),\quad \beta=\frac{r_0}{2\pi}\lambda^2 N_A\sum_i\frac{\rho_i}{A_i}f_i'' , \tag{1}$$

where the summation is over all the constituent elements i; $r_0=e^2/mc^2$ is the classical radius of electron; N_A is

Avogadro's number; ρ is the mass density; A and Z are atomic weight and number, respectively, and f' and f'' are the anomalous scattering factors. The refractive index being slightly smaller than unity means that the material appears to x rays as a dilute medium compared to air, i.e., it can totally reflect the x ray at incidence angles smaller than the critical angle $\theta_c=(2\delta)^{1/2}$. The complex refractive index indicates that propagation of x ray with grazing-incidence angle θ can be described by a plane wave with complex wave vector $P_z=k\sqrt{n^2-\cos^2\theta}$, i.e., the amplitude of the plane wave is attenuated in the material, and $k=2\pi/\lambda$ is the wave vector in vacuum.

Transmission and reflection of x rays at an interface can be calculated by following Fresnel's laws in classic optics,[12-14] and the effects of interfacial roughness can be incorporated using a vector scattering model by Vidal and Vincent.[15] In this model a parameter σ_i representing the root-mean-square (rms) roughness at the ith interface is introduced and deviations of interfacial height from an ideal planar boundary are assumed to follow a normal Gaussian distribution. The net effect of x-ray reflection from such a rough surface amounts to a simple modification of the usual reflectivity with an additional Debye-Waller-like factor.

For multilayer structures, there are several approaches to calculate the specular reflectivity, such as the recursion[13,16] and matrix formulation,[17] etc. These different mathematical approaches yield the same results since they are based on the same physical principles using the Maxwell equations and same boundary conditions for the electromagnetic fields at the interface. In the present work the matrix formulation has been used to compute the fields and flux distribution inside the layered structures, which gives directly the specular reflectivity for comparison with our experimental data. The fluorescence yield is calculated using the same approach, after incorporating a model for the density profile of the fluorescent atoms.

Consider the electric fields at the interface between the ith and $(i+1)$th layers; they are governed by Fresnel's reflection and transmission coefficients for smooth surfaces. For a rough interface, the coefficients are then modified by a Debye-Waller-like factor. Assuming s polarization (the x-ray electric field perpendicular to the scattering plane) and the rms roughness to be σ_i, the electric fields on the two sides of this interface are related through a matrix as

$$\begin{bmatrix} E_i^+(z_i) \\ E_i^-(z_i) \end{bmatrix} = \frac{1}{t_i'} \begin{bmatrix} 1 & r_i' \\ r_i' & 1 \end{bmatrix} \begin{bmatrix} E_{i+1}^+(z_i) \\ E_{i+1}^-(z_i) \end{bmatrix} , \tag{2}$$

where z_i is the mean position of interface i, and E_i^+ and E_i^- are transmitted and reflected fields in layer i; $r_i'=r_i\exp(-2p_{zi}p_{zi+1}\sigma_i^2)$ and $t_i'=t_i/\exp[-(p_{zi}-p_{zi+1})^2\sigma_i^2]$, where r_i and t_i are Fresnel's reflection and transmission coefficients for a smooth interface. The transmitted and reflected electric fields in the same layer are related to each other by a propagation matrix

$$\begin{bmatrix} E_i^+(z_i) \\ E_i^-(z_i) \end{bmatrix} = \begin{bmatrix} e^{-ip_{zi}(z-z_i)} & 0 \\ 0 & e^{ip_{zi}(z-z_i)} \end{bmatrix} \begin{bmatrix} E_i^+(z) \\ E_i^-(z) \end{bmatrix} ; \tag{3}$$

hence by successive operation of the matrices for all the interfaces and layers in the material, the net electric fields of the incident and reflected x rays are related to each other by a product matrix[17]

$$\begin{bmatrix} E_0^+ \\ E_0^- \end{bmatrix} = P_{0N} \begin{bmatrix} E_s^+ \\ 0 \end{bmatrix} = \begin{bmatrix} P_{0N}^{11} & P_{0N}^{12} \\ P_{0N}^{21} & P_{0N}^{22} \end{bmatrix} \begin{bmatrix} E_s^+ \\ 0 \end{bmatrix} , \tag{4}$$

where E_0^+ and E_0^- are the electric fields of the incident and reflected x rays at the top surface, respectively. E_s^+ is the electric field in the substrate where no reflected field is present. P_{0N} is the product of a series of matrices characteristic of the interfaces and epilayers. The reflectivity can be expressed in terms of the elements of matrix P_{0N},

$$R = \left| \frac{E_0^-}{E_0^+} \right|^2 = \left| \frac{P_{0N}^{21}}{P_{0N}^{11}} \right|^2 . \tag{5}$$

The electric field at any position inside the layered structure can also be related to the fields in the substrate by a manner similar to (4), so the electric-field distribution throughout the material can be readily obtained.

In the calculation of fluorescence yield we neglect the intensity loss due to Compton effect, phonon scattering, and other effects; the fluorescence yield intensity is then proportional to the intensity loss in the layered structure and the concentration of the fluorescent atoms. The intensity loss can be calculated using Poynting's theorem. Taking into account the density profile of fluorescent atoms (Ge in the present experiment) we obtain the fluorescence yield intensity[17,18]

$$J_{\mathrm{FY}} \propto \int dz \left[-\frac{dS_z(z)}{dz} \right] \Phi(z) , \tag{6}$$

where S_z is the z component of the Poynting's vector and $\Phi(z)$ is the density profile of fluorescent atoms. The integral is over the entire layered structure from the top surface to substrate.

Fresnel's laws of classical optics are only good for calculating specularly reflected and directly transmitted x rays; they cannot be applied in the treatment of diffuse scattering. Since the grazing-incidence angle is usually far away from critical angle θ_c and the scattering intensity is weak, it is appropriate to treat the scattering intensity in a weak-field approximation, i.e., using the Born approximation,[19] for calculating diffuse scattering. In the Born approximation the differential cross section for scattering of radiation by a system is given by

$$\frac{d\sigma}{d\Omega} = \int\int d\mathbf{r}\, d\mathbf{r}' \rho(\mathbf{r})\rho(\mathbf{r}') e^{-i\mathbf{q}\cdot(\mathbf{r}-\mathbf{r}')} , \tag{7}$$

where $\rho(r)$ is the density of scattering electrons, $\mathbf{q}=\mathbf{k}-\mathbf{k}_0$ is the scattering vector, and the integration is over the entire volume of the solid. Considering the layered structure and assuming a normal (Gaussian) distribution for height variations at the interface, the cross section for diffuse scattering can be expressed as[20]

$$\left[\frac{d\sigma}{d\Omega}\right]_{\text{diff}} = \frac{A}{16\pi^2}\sum_{i,j}\frac{\exp[-q_z^2(\sigma_i^2+\sigma_j^2)]}{q_z^2}F_{ij}e^{iq_z(z_i-z_j)}, \tag{8}$$

where A is the total surface area; σ_i and Z_i are the rms roughness and the mean position of ith interface; the summation is over all pairs of interfaces i and j; and

$$F_{ij}=\Delta\rho_i\Delta\rho_j\int\int dx\,dy(e^{q_z^2C_{ij}(x,y)}-1)e^{i(q_xx+q_yy)}, \tag{9}$$

where $\Delta\rho_i$ is the difference in the density of scattering electrons on two sides of the ith interface and

$$C_{ij}(x,y)=\langle\delta z_i(0,0)\delta z_j(x,y)\rangle=C_0(R)e^{-|Z_i-Z_j|/\xi_\perp} \tag{10}$$

is the correlation function between height fluctuations on interfaces i and j, respectively. $\delta z_i(x,y)$ is the height fluctuation on the ith interface at position (x,y) from an arbitrary origin, $R=\sqrt{x^2+y^2}$ is the distance from that origin; $C_0(R)$ is the in-plane correlation function which can be generally expressed as $\sigma_i\sigma_j\exp[-(R/\xi_\parallel)^{2h}]$; $\xi_\parallel$ and $\xi_\perp$ are the in-plane and cross-correlation lengths, respectively; and h is called a texture coefficient. From (8) we can see that there is a definite phase relation between different interfaces provided the cross-correlation length is reasonably large. If the interfacial roughness becomes uncorrelated (when the cross-correlation length is much less than the spacing between successive interfaces), C_{ij} vanishes for different interfaces $i\neq j$, and diffuse scattering is then a result of incoherent superposition of roughness scattering from each interface. When the roughness of different interfaces is correlated or conformal (when the cross-correlation length is comparable with or larger than the spacing between interfaces), it is possible to have a nonzero C_{ij} even for well-separated interfaces $i\neq j$. Thus the total diffuse scattering intensity can contain a coherent sum of scattering contributions from each interface, which will yield an interference pattern similar to that of specular scattering. The total diffuse scattering intensity is obtained by integrating over the detection solid angle to yield

$$I_{\text{diff}}\propto I_0\int d\Omega\left[\frac{d\sigma}{d\Omega}\right]_{\text{diff}}, \tag{11}$$

where I_0 is the flux of incident x rays.

III. EXPERIMENT

The x-ray measurements were carried out at X3B1 beamline at National Synchrotron Light Source (NSLS). The experimental setup is shown schematically in Fig. 1. The x-ray beam from the storage ring of NSLS is monochromatized by a Si(111) double-crystal monochromator and collimated by a set of slits. The intensity of the incident x-ray beam is monitored by an ionization chamber I_0 between slits $S2$ and $S3$. The intensity of x ray after scattering was measured by a NaI scintillation detector which has a slit $S4$ in front of it to define the angular resolution. The fluorescence yield was measured by an energy dispersive solid-state Si(Li) detector. The fluorescence detector was set at right angle to the scattering plane in order to suppress the elastic scattering. The layered structure specimen and the scattering detector were mounted on a two-circle goniometer whose rotation axis was controlled by a computer with 0.0002°/step precision. The experimental resolution was determined by the resolution of the monochromator and by the width of collimating slits. The incident beam was confined to 0.01° full width at half maximum (FWHM). The energy of the incident x-ray beam was set above the Ge K absorption edge at 11.5 keV in order to measure the scattering intensity and fluorescence yield simultaneously. Aluminum foils with different thickness were used to attenuate the incident beam during the measurements to obtain a range of up to 7 orders of intensity changes.

The geometry of our scattering experiment is shown in Fig. 2. The incident and scattered x-ray beams are at grazing angles α and β with respect to the sample surface, respectively [see Fig. 2(a)]. The scattering vector $\mathbf{q}$ is defined as the difference between the scattered and incident wave vectors,

$$\mathbf{q}=\mathbf{k}-\mathbf{k}_0 . \tag{12}$$

Let z be the direction normal to the sample surface and x be parallel to the surface plane; the scattering vector can be resolved into perpendicular and in-plane components q_z and q_x,

$$q_x=k(\cos\beta-\cos\alpha),\quad q_z=k(\sin\beta+\sin\alpha), \tag{13}$$

where $k=2\pi/\lambda$ is the wave vector of radiation in vacuum. Three different scans were performed during the measurements: (a) specular scattering scans in which the incident angle α is kept equal to the observation angle β, i.e., scattering vector is always normal to the sample surface so that $q_x=0$; (b) longitudinal diffuse scattering scans in which the observation angle is off the direction of specular reflection by a small but constant angle δ, hence the scattering vector has a nonzero component in the sample surface plane; and (c) transverse diffuse scattering scans in which the detector was fixed at a cer-

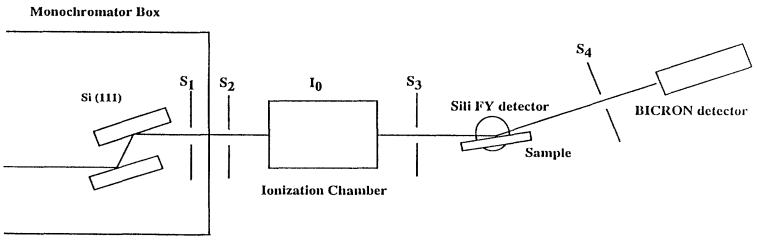

FIG. 1. Schematic arrangement of the experimental setup at beamline X3B1 of NSLS. The monochromator is a Si(111) double crystal. The exit slit $S1$ defines the coarse horizontal and vertical size of the incident x-ray beam; fine size definition of beam is controlled by the slits $S2$ and $S3$.

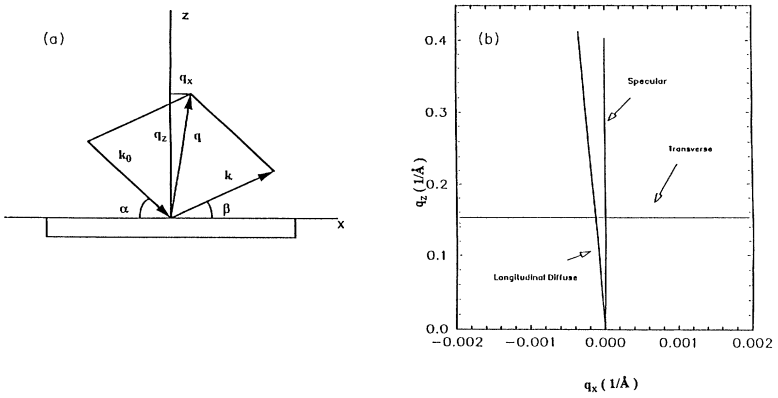

FIG. 2. (a) Schematic representation of the scattering vector $\mathbf{q}$. $\mathbf{k}_0$ and $\mathbf{k}$ are the incident and scattered wave vectors of the x-ray beam, respectively. Scattering vector $\mathbf{q}=\mathbf{k}-\mathbf{k}_0$ represents the momentum transfer of x-ray photons. $\mathbf{q}_x$ and $\mathbf{q}_z$ are the in-plane and perpendicular components of the scattering vector. (b) Representation of different angular scans in the reciprocal space.

tain angle and the sample is rocked through the configuration of specular reflection, such that the scattering vector has a constant perpendicular component q_z. These three different scans are shown as different cuts in the reciprocal space in Fig. 2(b). We note that the specular and longitudinal diffuse scans are used to probe the structure normal to the sample surface since the variation of scattering vector is largely perpendicular to the sample plane, whereas the transverse diffuse scans are used to investigate the structure parallel to the sample surface since the variation of scattering vector is in this plane.

As shown in Eqs. (8)–(10), the longitudinal diffuse scan can provide unique structural information about the correlation of interfacial roughness between different interfaces. In addition, it allows an important correction to be made for the measured reflectivity in the specular scan which actually contains a contribution from the background due to diffuse scattering by interfacial roughness. In order to obtain the true specular reflectivity, this diffuse background must be properly subtracted out; otherwise the global roughness deduced from the specular reflectivity data will be underestimated. The diffuse scattering intensity at small incidence angles is generally several orders weaker than the specular reflectivity and it also shows a broad peak in the same scattered direction as the specular reflection; this can be clearly observed in a transverse scan. Hence, to a good approximation, the diffuse background correction in the measured specular reflectivity can be achieved by simply subtracting the diffuse scattering obtained at an angle slightly off the $q_x=0$ direction from the specular reflectivity curve. This method has been used to correct for all the specular reflectivity data obtained in the present experiment.

The layered materials studied in the present experiment are $Si_{1-x}Ge_x$/Si heterostructures and superlattices (MBE) molecular-beam epitaxy grown on Si(100) substrates. Two heterostructures JP187F and JP186F are called normal and inverted structures, respectively. The sample JP187F is a $Si_{0.7}Ge_{0.3}$ epilayer with nominal thickness 100 Å grown on a Si(100) wafer with a 3000-Å Si buffer layer. The sample JP186F has an additional Si epilayer with nominal thickness of 100 Å on top of the $Si_{0.7}Ge_{0.3}$ layer than JP187F. The first interface in JP187F is a normal heterostructure $Si_{0.7}Ge_{0.3}$/Si and that in JP186F is an inverted structure Si/$Si_{0.7}Ge_{0.3}$. Two superlattices JP2 and JP121F studied each consists of ten-period Si(100 Å)/$Si_{0.8}Ge_{0.2}$(70 Å) and $Si_{0.6}Ge_{0.4}$(45 Å)/Si(300 Å) bilayers; JP2 has a 1000-Å Si buffer layer and JP121F has a 500-Å Si cap layer, respectively. Based on the previous results on $Si_{1-x}Ge_x$ epitaxial layers,[21,22] the critical thickness of the $Si_{1-x}Ge_x$ layer is estimated to be about 2500, 500, and 200 Å for $x=0.2$, 0.3, and 0.4, respectively. The thickness of all the $Si_{1-x}Ge_x$ layers in our samples is below the critical thickness for the corresponding composition. This means that all the epilayers are expected to be pseudomorphic.

IV. RESULTS AND DISCUSSION

Scans of specular reflection, longitudinal and transverse diffuse scattering have been made. The true specular reflectivity of the samples was obtained by subtracting the measured longitudinal diffuse scattering contributions from the raw specular reflection data. The structural parameters of the samples, such as the layer thickness, interfacial roughness, and optical constants were deduced from these data by means of a nonlinear least-squares curve-fitting technique. In order to increase the sensitivity to the oscillations caused by interference of scattering from different interfaces, we have fitted the raw data as well as their angular derivatives simultaneously such that the following quantity was minimized during each curve fitting:

$$\chi^2=\chi_1^2+c\chi_2^2 , \tag{14}$$

where χ_1^2 is the mean square of the difference between the raw data and corresponding theoretical calculation, χ_2^2 is the mean square of the difference between the first derivative of raw data and its corresponding calculated value, and c is a constant that adjusts the weight of derivatives in the fitting procedure. For a good fit, the resulting parameters should be essentially independent of the choice of c value because a good model should fit the experimental data as well as their derivatives equally well. The errors for each parameter determined by curve fitting were estimated from the deviation of that parameter from its optimum value. This estimate of errors for a particular parameter P_i was carried out in the following steps:

TABLE I. Structural parameters of four samples obtained in the present work by comparison of experimental data with theoretical calculations. N is the number of epilayers in semiconductor material; D_0 is the thickness of the cap layer on the sample; D_1 is the thickness of the Si epilayer; D_2 is the thickness of the SiGe epilayer; σ_0 is the rms roughness parameter for the top surface; σ_1 is the rms roughness parameter for the Si/SiGe interface; σ_2 is the rms roughness parameter for the SiGe/Si interface; h is the texture coefficient in the epilayer; $\xi_{\parallel}$ is the in-plane correlation length. A dash means that the value is not available.

Sample	N	D_0 (Å)	D_1 (Å)	D_2 (Å)	σ_0 (Å)	σ_1 (Å)	σ_2 (Å)	h	$\xi_{\parallel}$ (Å)
JP187F	1	—	—	77±2	4±1	—	3±2	0.47	700
JP186F	2	—	115±2	97±2	4±1	4±2	5±2	0.47	870
JP121F	21	353	352	51	4	5	4	0.45	6000
JP2	20	—	116	69	9	10	12	—	—

select a certain deviation ΔP_i for P_i from its optimum value, and minimize χ^2 by varying all the other parameters in the model except for P_i; this process was repeated by changing ΔP_i until the new minimized χ^2 became twice the optimal minimum value of χ^2; this particular ΔP_i was then taken as the error in the value of the parameter P_i determined in curve fitting. Results obtained for the four samples studied in the present experiment are summarized in Table I.

A. Normal and inverted heterostructures

Figure 3(a) shows the corrected true specular reflectivity and longitudinal diffuse scattering data for both the normal and inverted heterostructures JP187F and JP186F, respectively. The circles are the true specular reflectivity after subtracting out the longitudinal diffuse scattering contributions from the raw data; the solid lines on the circles are theoretical calculations using Eq. (5); the solid curve underneath each specular reflectivity curve is longitudinal diffuse scattering measured by offsetting the detector from the specular direction by an angle of 0.1°. In the curve-fitting process, the layer thickness and interfacial roughness are the structural parameters determined from these data. The initial trial values of optical constants for each constituent material were calculated using Cromer and Liberman's methods[23] for the SiGe alloys. The optical constants are subject to corrections for layered structures and also for strain-induced changes in these thin layers; the correct values of these optical constants are finally determined from the experimental data. In the curve-fitting process, reasonable initial values were first chosen for the layer thickness, interfacial roughness, and the optical constants, and these quantities were all consistently adjusted through iterations to reach a final fit to the experimental reflectivity data.

For the sample JP187F, which has only a $Si_{0.7}Ge_{0.3}$ epilayer, there are oscillations with a single frequency arising from the interference of x rays reflected from the top surface and the $Si_{0.7}Ge_{0.3}$/Si interface. The oscillation frequency is primarily determined by the thickness of the $Si_{0.7}Ge_{0.3}$ layer and the intensity is mainly determined by the optical contrast (mismatch of the optical constants), x-ray absorption in the epilayer, and roughness of the interface as well as the top surface. As shown in Table I, the thickness of the $Si_{0.7}Ge_{0.3}$ layer is found to be 77±2 Å, which is quite different from the nominal thickness based on an estimate during epitaxial growth. The roughness parameter for the top surface is 4±1 Å, and that for the $Si_{0.7}Ge_{0.3}$/Si interface is 3±2 Å, indicating that the epilayer is very smooth. The roughness parameter for the top surface is more accurately determined than that of the interface because x-ray scattering is more sensitive to the morphology of the top surface than the interfacial microstructure. The longitudinal diffuse scattering data do not show any oscillatory feature as in the specular reflectivity. In accordance with Eq. (10), this implies that the cross-correlation length $\xi_{\perp}$ is much smaller than the layer thickness in this sample such that the coefficient C_{ij} with $i \neq j$ is vanishingly small; x rays scattered from the two interfaces bear no phase correlation, indicating that height fluctuations of the top surface and the interface roughness are uncorrelated (or nonconformal) in this heterostructure.

In the reflectivity curve for sample JP186F, there are beating patterns of the oscillations as a result of x-ray interference in the Si and $Si_{0.7}Ge_{0.3}$ thin layers of this sample. Scattering from these two thin layers (three interfaces) all contribute to the total measured scattering. As shown in Table I, the thickness of Si and $Si_{0.7}Ge_{0.3}$ layers was found to be 115±2 and 97±2 Å, respectively. The roughness parameter for the Si/$Si_{0.7}Ge_{0.3}$ and $Si_{0.7}Ge_{0.3}$/Si interface is 4±2 and 5±2 Å while that of the top surface is 4±1 Å, respectively. In comparison with similar parameters of sample JP187F, roughness for the normal interface $Si_{0.7}Ge_{0.3}$/Si in JP187F and inverted interface Si/$Si_{0.7}Ge_{0.3}$ in JP186F is very close. In fact, the second interface in sample JP186F is a normal $Si_{0.7}Ge_{0.3}$/Si interface, although the roughness value for this interface is 5±2 Å. The longitudinal diffuse scattering data also do not exhibit any oscillations, consistent with the short cross-correlation length found in sample JP187F.

The sensitivity of this technique for the determination of interfacial roughness parameter σ is actually quite high, with a resolution on the order of 2 Å. This is demonstrated in a model calculation using the heterostructure JP187F as an example. Three calculated curves are shown in Fig. 3(b) together with the experimental data. In the calculations, the thickness and all physical constants pertaining to the layers are kept the same ex-

cept for the interfacial roughness parameter which assumes the value of $\sigma = 0$, 3, and 5 Å, respectively. The middle curve with $\sigma = 3$ Å gives the best fit to the experimental data.

Considering the experimental and curve-fitting errors, the normal and inverted interfaces between $Si_{0.7}Ge_{0.3}$ and Si both show quite similar low values of rms roughness, indicating that these MBE-grown heterostructures are all very smooth. These results provide a convincing evidence that high-quality SiGe/Si superlattices can indeed be grown epitaxially for various device applications.

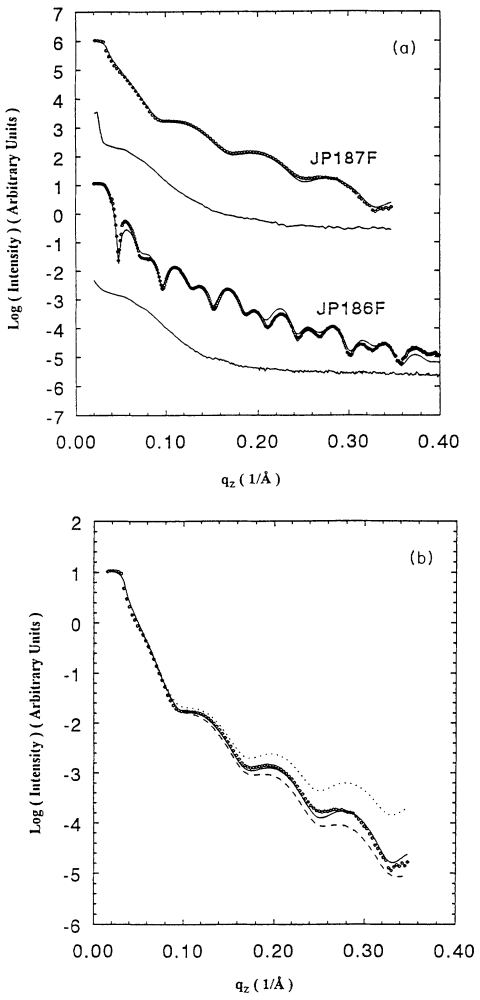

FIG. 3. (a) The corrected true specular reflectivity and longitudinal diffuse scattering for two heterostructure samples: JP187F and JP186F. Circles are specular reflectivity after subtracting out the longitudinal diffuse scattering contributions; the solid lines on the data are theoretical calculations used to fit the data. The solid curves underneath the specular reflectivity for each sample are the longitudinal diffuse scattering data, measured with the detector set at an angle 0.1° off the direction of specular reflection. The logarithm is in base 10. (b) Model calculations of specular reflectivity for JP187F in comparison with experimental data (circles). The calculated curves were obtained by using the same thickness and physical constants of the layers except for different roughness parameters: $\sigma = 0$ Å (dotted curve), 3 Å (solid curve), and 5 Å (dashed curve). The solid curve gives the best fit to the data.

The transverse diffuse scattering data for samples JP187F and JP186F are shown in Fig. 4. The central peak is due to specular reflection and its width is determined by the angular resolution of the experimental setup. The background of transverse diffuse scattering is determined by the interfacial roughness and in-plane correlation of height fluctuations. The calculated diffuse scattering intensity using Eqs. (8)–(10) based on Born approximation is also shown in Fig. 4 as a solid curve for each sample. In our experiment, the incident beam was confined in the vertical direction with a slit about 0.1 mm wide while the horizontal direction was wide open; this configuration has in effect performed one integral in (9). The calculation therefore reduces to a one-dimensional integral to evaluate the diffuse scattering intensity. Equation (9) is actually a Fourier transform, hence a fast-Fourier-transform routine can be readily used to calculate the integral in (9). From the close fit to the experimental data in Fig. 4, the results give the same value of the texture coefficient $h = 0.47$ for both samples, and the in-plane correlation length is 700 and 870 Å for JP187F and JP186F, respectively.

The measured (circles) and calculated (solid line) angular dependence of Ge $K\alpha$ fluorescence yield are shown in Fig. 5. At grazing-incidence angles smaller than the critical angle, x rays are totally reflected by the sample, only the evanescent fields penetrate into the material, and the fluorescence yield (FY) is very small. The sample JP187F contains Ge in the top $Si_{0.7}Ge_{0.3}$ layer; hence it shows stronger FY even at very low grazing angle than JP186F, in which the top layer contains no Ge atoms. The x ray penetrates deeper as the grazing angle increases beyond the critical angle; therefore FY increases very quickly with the grazing angle for both samples. However, for thin films grown on a substrate, the flux distribution of photons depends on the field pattern inside the film on ac-

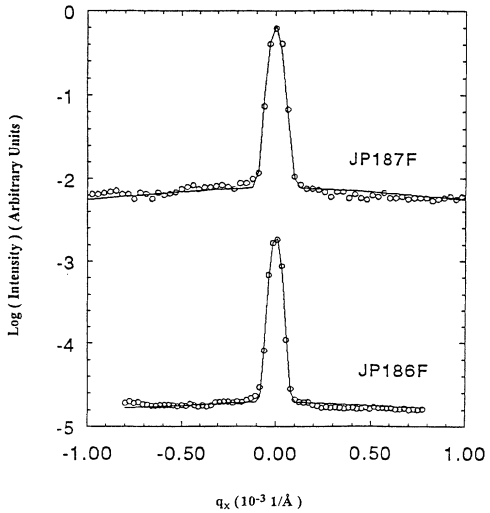

FIG. 4. The measured (circles) and calculated (solid lines) transverse diffuse scattering vs in-plane momentum transfer for the heterostructures JP187F and JP186F.

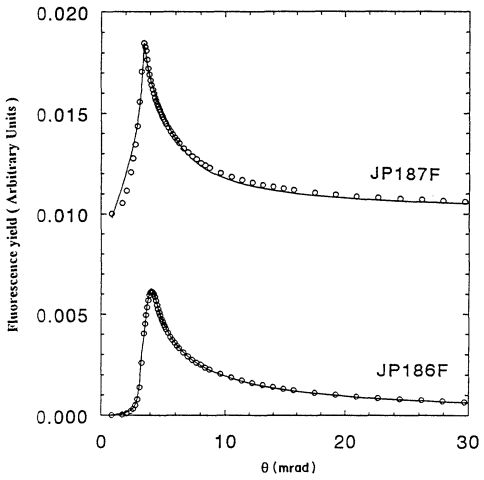

FIG. 5. The measured (circles) and calculated (solid lines) fluorescence yield vs grazing-incidence angle for the heterostructures JP187F and JP186F. The plot for JP187F has been shifted up by 0.01 for clarity.

count of the incoming and reflected waves. A large portion of the x-ray flux can penetrate through the layers into the substrate when the grazing angle is larger than the critical angle. The intensity within the $Si_{0.7}Ge_{0.3}$ layer begins to decrease as this condition prevails, thereby giving rise to a decrease of the Ge FY at large angles. This generally explains the existence of a peak in the angular dependence of FY for layered materials.

The overall angular variation of Ge FY for both samples JP187F and JP186F can be quantitatively explained with a calculation of the flux distribution in the layered materials. In Fig. 6, the calculated photon flux distribution as a function of depth in both heterostructure samples is shown for different grazing-incidence angles θ below ($\theta=\theta_c/2$, dashed), equal ($\theta=\theta_c$, solid), and above ($\theta=2\theta_c$, dashed dot) the critical angle. The FY intensity is mainly determined by the field intensity in the SiGe layer according to Eq. (6). In this calculation of Ge $K\alpha$ FY, we have also used the structural parameters obtained from the reflectivity data and assumed a step function for the Ge density profile $\Phi(z)$ in (6). This calculation is also employed to fit the experimental FY data in Fig. 5. The close fit for both samples shown in Fig. 5 suggests that Ge atoms should not deviate appreciably from a uniform distribution in the $Si_{0.7}Ge_{0.3}$ layers and diffusion of Ge atoms into the Si layer could be negligible within the experimental uncertainty of this method. More detailed analysis is in progress.

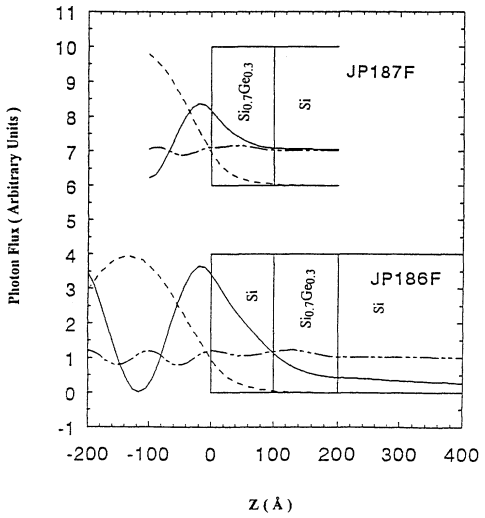

FIG. 6. Calculated photon flux distribution in the heterostructures JP187F and JP186F for different grazing-incidence angles: $\theta=\theta_c/2$ (dashed), $\theta=\theta_c$ (solid), and $\theta=2\theta_c$ (dashed dots).

B. Superlattices

The specular reflectivity and longitudinal diffuse scattering data obtained with two superlattices JP121F and JP2 are shown in Fig. 7. The longitudinal diffuse scattering measurements were made at a small angle 0.1° off the direction of specular reflection. The specular reflectivity data were fitted with calculations using Eqs. (2)–(5) based on Fresnel's laws. The structural parameters determined from curve fitting are shown in Table I. In order to reduce the number of fitting parameters in our calculation, the optical constants are assumed to be the same for all the layers with same composition in the superlattices. The average thickness and SiGe/Si interfacial roughness of the epilayers were determined from the data, but possible variations of these quantities in the superlattices were neglected in this calculation as they were all grown under identical processing conditions.

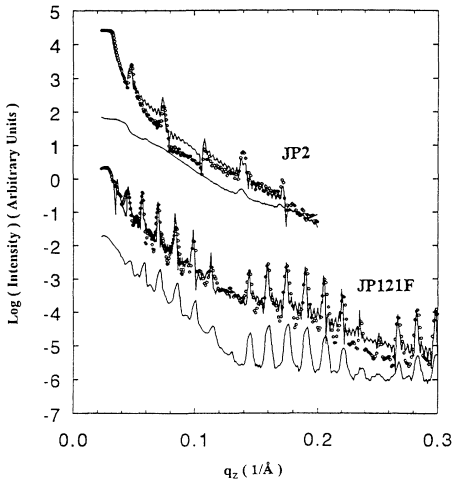

FIG. 7. The corrected true specular reflectivity and longitudinal diffuse scattering for two superlattice samples JP2 and JP121F. Circles are specular reflectivity after subtracting out the longitudinal diffuse scattering contributions; solid lines on the data are theoretical calculations used to fit the data. The solid curves underneath the specular reflectivity for each sample are longitudinal diffuse scattering measured with the detector set at an angle 0.1° off the direction of specular reflection.

Since both superlattices contain SiGe/Si bilayers, Bragg diffraction peaks and beating patterns are expected to be present in the reflectivity data. For the sample JP121F, beating is clearly observed as manifested by the intensity variation with a minimum separating approximately every seven maxima. This relationship is consistent with the thickness ratio of the layers estimated during epitaxial growth. A similar type of beating pattern is also found in the reflectivity data of sample JP2 where some Bragg peaks are suppressed due to destructive interference. Because the thickness of the SiGe/Si bilayers is relatively small (170 Å) in JP2, the q_z spacing between successive Bragg peaks of this multilayer is larger than that in JP121F. It is interesting to note that small oscillations due to interference caused by the thickness of the entire multilayer sample can also be observed; this gives rise to $N-1$ small oscillations for a superlattice consisting of N bilayers. For JP2 with $N=10$, there are indeed nine small minima between two successive main Bragg peaks arising from interference due to neighboring bilayers. This also serves as an indication of the high angular resolving power of our experimental setup.

In Fig. 7, the longitudinal diffuse scattering data are shown in solid curves underneath that of the specular reflectivity. We note the presence of apparent interference patterns in these plots, especially for the superlattices JP121F. To make sure that these longitudinal scattering scans do not pick up any of the specular reflection signal, the detector was offset at an angle far away from the direction of specular reflection, typically 4–5 times larger than the FWHM of the specular reflection peaks. Furthermore, the longitudinal diffuse scattering was measured at different offset angles of 0.1°, 0.2°, and −0.1° for comparison. All these measured diffuse scattering data produced similar interference patterns. This is demonstrated in Fig. 8 specifically for the sample JP121F at two different detector offsets: 0.1° (solid curve) and 0.2° (dots), which clearly show similar

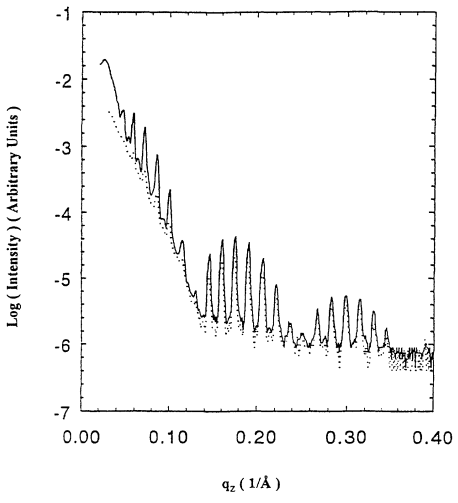

FIG. 8. The measured longitudinal diffuse scattering with different detector offsets δ for superlattice JP121F: δ=0.1° (solid curve) and δ=0.2° (dots).

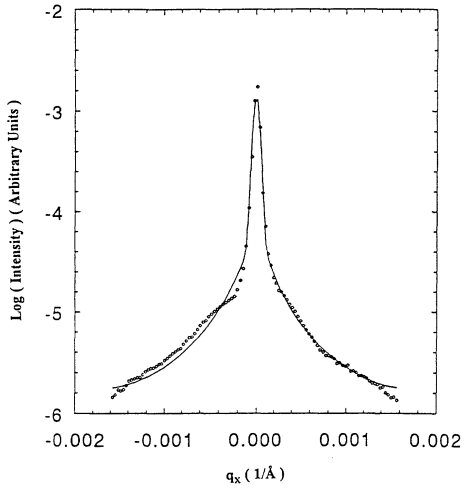

FIG. 9. The measured (circles) and calculated (solid line) transverse diffuse scattering for the superlattice JP121F vs in-plane momentum transfer. The measurements were made with the detector set at a scattering angle $2\theta=\alpha+\beta=1.718°$, on the tenth main Bragg peak in the specular reflectivity.

interference patterns in these two sets of longitudinal diffuse scattering data. These results unequivocally indicate that the interfaces in this superlattice sample are conformal, thus x rays scattered from different interfaces remain coherent with a fixed phase relation. This also implies that the cross-correlation length between different interfaces is larger than the layer thickness in JP121F. These results suggest that JP121F has a better structural quality than JP2; this is also consistent with the different measured values of interfacial roughness in these two superlattices.

The transverse diffuse scattering data obtained with sample JP121F are shown in Fig. 9. These are measured by fixing the detector at an angle corresponding to the tenth main Bragg peak in the specular reflectivity. A model calculation is also shown in Fig. 9 (solid curve), which fits the data reasonably well. The in-plane correlation length and texture coefficient h derived from this comparison are included in Table I. The texture coefficient of this superlattice is nearly the same as that of both heterostructures JP187F and JP186F, although the in-plane correlation length is much larger than that of the heterostructures. These results reveal that the in-plane microstructures of SiGe/Si interfaces in both heterostructures and superlattices are very similar. Hence high-quality SiGe/Si superlattices with abrupt interfaces can indeed be grown under proper conditions.

V. CONCLUSION

X-ray scattering and fluorescence measurements have been demonstrated as useful nondestructive techniques for measuring the layer thickness and for investigating the microstructures in semiconductor heterostructures and superlattices. The specular reflectivity, diffuse scattering, and fluorescence yield techniques have been

applied to the study of two SiGe/Si heterostructures grown by MBE with normal and inverted interfaces, and the results show these two heterostructures are of similar high quality in terms of their rms interfacial roughness parameters. However, for these thin bilayer samples, the cross-correlation lengths are smaller than the total layer thickness although their in-plane correlation lengths are similar. The fluorescence data are consistent with an assumption that diffusion of Ge into the Si layer is negligible in both heterostructures.

The same techniques are also shown to be very useful for investigating semiconductor superlattices, from which the layer thickness, interfacial roughness, cross- and in-plane correlation lengths have been determined. The superlattices show high quality of interfacial structures and correlations between height fluctuations of different interfaces.

ACKNOWLEDGMENTS

The present research at SUNY Buffalo was supported by DOE. The work at UCLA was supported by ARO and ONR. One of us (Z.H.M.) would like to thank Dr. K. G. Huang of Argonne National Laboratory for helpful discussions. The experiments were carried out at NSLS Beamline X3 supported by DOE.

[1]R. People, IEEE J. Quantum Electron. **QE-22**, 1696 (1986); G. M. W. Kroesen *et al.*, Appl. Phys. Lett. **60**, 1351 (1992).
[2]E. Glaser *et al.*, Phys. Rev. Lett. **65**, 1247 (1990).
[3]R. People *et al.*, Appl. Phys. Lett. **45**, 1231 (1984).
[4]D. V. Lang, R. People, J. C. Bean, and A. M. Sergent, Appl. Phys. Lett. **47**, 1333 (1985).
[5]G. C. Osbourn, J. Vac. Sci. Technol. B **2**, 176 (1984).
[6]C. R. Bolognesi, H. Kroemer, and J. H. English, Appl. Phys. Lett. **61**, 213 (1992).
[7]J. W. Matthews and A. E. Blakeslee, J. Cryst. Growth **27**, 118 (1974); J. Petrucello, O. J. Olego, X. Chu, and J. P. Faurie, J. Appl. Phys. **63**, 1783 (1988).
[8]M. Tanaka and H. Sasaki, J. Cryst. Growth **81**, 153 (1981); M. Tanaka, H. Sasaki, J. Yoshino, and T. Furuta, Surf. Sci. **174**, 65 (1986).
[9]D. D. Allred, J. Gonzalez-Hernandez, O. V. Nguyen, D. Martin, and D. Pawlik, J. Mater. Res. **1**, 468 (1986); P. D. Persans, A. F. Ruppert, B. Ableles, and T. Tiedje, Phys. Rev. B **32**, 5558 (1985).
[10]For a general reference, see, for example, R. W. James, *The Optical Principles of the Diffraction of X-rays* (Ox Bow, Woodbridge, 1982).
[11]D. L. Henke, P. Lee, T. J. Tanaka, R. L. Shimabukuro, and B. K. Fujikawa, At. Data Nucl. Data Tables **27**, 1 (1982).
[12]M. Born and E. Wolf, *Principles of Optics* (Pergamon, New York, 1965).
[13]L. G. Parrat, Phys. Rev. **35**, 359 (1954).
[14]A. B. Braslau, P. S. Pershan, G. Swislow, B. M. Ocko, and J. Als-Nielsen, Phys. Rev. A **38**, 2457 (1988).
[15]B. Vidal and P. Vincent, Appl. Opt. **23**, 1794 (1984).
[16]H. Chen and S. M. Heald, J. Appl. Phys. **66**, 1793 (1989).
[17]A. Krol, C. Sher, and Y. H. Kao, Phys. Rev. B **38**, 8579 (1988).
[18]D. K. G. de Boer, Phys. Rev. B **44**, 498 (1991).
[19]S. K. Sinha, E. B. Sirota, S. Garott, and H. B. Stanley, Phys. Rev. B **38**, 2297 (1988).
[20]S. K. Sinha, Physica B **173**, 25 (1991).
[21]J. C. Bean, L. C. Feldman, A. T. Fiory, S. Nakahara, and I. K. Robinson, J. Vac. Sci. Technol. A **2**, 436 (1984).
[22]R. People and J. C. Bean, Appl. Phys. Lett. **47**, 322 (1985).
[23]D. T. Cromer and D. A. Liberman, J. Chem. Phys. **53**, 1891 (1970); Acta Crystallogr. Sec. A **37**, 267 (1981).